Electrode Effect on Ferroelectricity in Free-Standing Membranes of PbZr$_{0.2}$Ti$_{0.8}$O$_3$

Qiuchen Wu, Kun Wang, Alyssa Simpson, Yifei Hao, Jia Wang, Dawei Li, and Xia Hong*

Read Online

ACCESS | Metrics & More | Article Recommendations | Supporting Information

ABSTRACT: We report the effects of screening capacity, surface roughness, and interfacial epitaxy of the bottom electrodes on the polarization switching, domain wall (DW) roughness, and ferroelectric Curie temperature (T_C) of PbZr$_{0.2}$Ti$_{0.8}$O$_3$ (PZT)-based free-standing membranes. Singe crystalline 10−50 nm (001) PZT and PZT/La$_{0.67}$Sr$_{0.33}$MnO$_3$ (LSMO) membranes are prepared on Au, correlated oxide LSMO, and two-dimensional (2D) semiconductor MoS$_2$ base layers. Switching the polarization of PZT yields nonvolatile current modulation in the MoS$_2$ channel at room temperature, with an on/off ratio of up to 2×10^5 and no apparent decay for more than 3 days. Piezoresponse force microscopy studies show that the coercive field E_c for the PZT membranes varies from 0.75 to 3.0 MV cm^{-1} on different base layers and exhibits strong polarization asymmetry. The PZT/LSMO membranes exhibit significantly smaller E_c, with the samples transferred on LSMO showing symmetric E_c of about −0.26/+0.28 MV cm^{-1}, smaller than that of epitaxial PZT films. The DW roughness exponent ζ points to 2D random bond disorder dominated DW roughening ($\zeta = 0.31$) at room temperature. Upon thermal quench at progressively higher temperatures, ζ values for PZT membranes on Au and LSMO approach the theoretical value for 1D random bond disorder ($\zeta = 2/3$), while samples on MoS$_2$ exhibits thermal roughening ($\zeta = 1/2$). The PZT membranes on Au, LSMO, and MoS$_2$ show T_C of about 763 ± 12, 725 ± 25, and 588 ± 12 °C, respectively, well exceeding the bulk value. Our study reveals the complex interplay between the electrostatic and mechanical boundary conditions in determining ferroelectricity in free-standing PZT membranes, providing important material parameters for the functional design of PZT-based flexible nanoelectronics.

KEYWORDS: free-standing PZT membranes, ferroelectric hysteresis, depolarization, domain wall roughness, ferroelectric field effect transistors
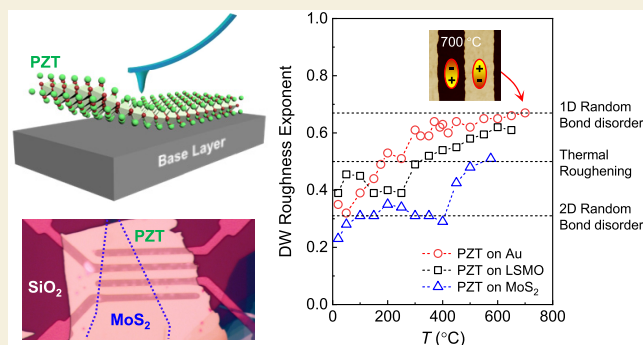
1. INTRODUCTION

Free-standing ferroelectric oxide membranes have attracted extensive research interests recently as they provide a versatile playground to explore low dimensional ferroelectricity and corrugation-enabled flexoelectricity.[1−3] Being free of the clamping effect from the epitaxial substrates, crystalline oxide membranes based on PbTiO$_3$, Pb(Zr,Ti)O$_3$, BaTiO$_3$, and their heterostructures exhibit various exotic properties, such as slow domain wall (DW) motion,[4] unconventional electromechanical coupling,[5,6] enhanced piezoelectric coefficient,[7] and bubble domain formation[8,9] that can be reversibly switched by an electric field.[8] The flexible nature also facilities strain engineering via stretchable or corrugated base layers, which leads to substantial modulation of their bandgap,[10] coercive field (E_c),[11,12] dielectric permittivity,[12] ferroelastic domains,[13] and photovoltaic response.[14] Unlike epitaxial complex oxide heterostructures, whose preparation imposes stringent requirements for the structural similarity between the constituent layers,[15] ferroelectric oxide membranes can be easily integrated

with the mainstream Si platform[12,16,17] and two-dimensional (2D) van der Waals materials[18,19] for developing flexible nanoelectronics, optics, and energy applications.[3,20,21] It also possesses distinct advantages compared with ferroelectric polymers[22] and 2D van der Waals ferroelectrics[23] for its high Curie temperature (T_C), large polarization (P), and scalable synthesis. A wide range of device concepts have been realized based on ferroelectric oxide membranes, including ferroelectric tunnel junctions,[16,17,24] ferroelectric field effect transistors (FETs),[19] reconfigurable optical filters,[18] DW memories,[25] and supercapacitors.[26]

For perovskite oxides, the type of electrode has a significant impact on T_C, polarization dynamics, domain formation, and size scaling because the ferroelectric instability depends sensitively on the depolarization field,[27,28] strain,[29] and defect states.[30] These factors are strongly entangled in epitaxial thin films,[31] while free-standing membranes present an ideal platform to decouple the individual contributions of polarization screening, curvature induced flexoelectricity, lattice distortion, and interfacial epitaxy.[1,6,13] To date, the effects of electrode imposed electrostatic and mechanical boundary conditions on ferroelectricity in complex oxide membranes remain elusive, and an in-depth understanding can facilitate the design of novel polar states in this intriguing material system as well as promote its technological implementation.

Here, we report a comprehensive study of polarization switching and DW configuration in free-standing PbZr$_{0.2}$Ti$_{0.8}$O$_3$ (PZT) and PZT/La$_{0.67}$Sr$_{0.33}$MnO$_3$ (LSMO) membranes transferred on three types of conductive electrodes with distinct screening capacity: the metallic Au, strongly correlated oxide LSMO, and 2D semiconductor MoS$_2$. A nonvolatile current on/off ratio of up to 2×10^5 has been achieved in the MoS$_2$ channel at room temperature via switching the polarization of the PZT top-layer with no apparent decay for more than 3 days. Piezoresponse force microscopy (PFM) switching hysteresis shows that the E_c depends sensitively on the bottom electrode type, varying from 0.75 to 3.0 MV cm^{-1} for the PZT membranes and from 0.18 to 1.01 MV cm^{-1} for the PZT/LSMO membranes, with the latter being smaller than that of epitaxial PZT films. The DW roughness exponent ζ points to 2D random bond (RB) disorder dominated DW roughening ($\zeta = 0.31$) at room temperature, which evolves to 1D RB disorder ($\zeta = 2/3$) dominated behavior for PZT membranes on Au and LSMO and thermal roughening ($\zeta = 1/2$) for samples on MoS$_2$ upon thermal quench at high temperatures. The PZT membranes on Au, LSMO, and MoS$_2$ show T_C of about 763 ± 12, 725 ± 25, and 588 ± 12 °C, respectively, well exceeding the bulk value. Our study reveals the complex interplay among the polarization screening capacity, surface roughness, and interface chemical bonding of the bottom electrodes in determining ferroelectricity of free-standing PZT membranes, providing important material parameters for the functional design of PZT-based flexible nanoelectronics.

2. RESULTS AND DISCUSSION

2.1. Sample Preparation and Characterization

We deposit 10−50 nm epitaxial PZT thin films and PZT/10 nm LSMO heterostructures on 20 nm Sr$_3$Al$_2$O$_6$ (SAO) buffered (001) SrTiO$_3$ (STO) substrates (Figure 1a). After water etching of the SAO layer, the suspended membranes are transferred on three types of conductive base layers: 20−50 nm Au deposited on SiO$_2$/Si, 20 nm epitaxial LSMO deposited on (001) STO, and few layer (FL) MoS$_2$ transferred on SiO$_2$/Si (Figure 1b), which serve as the bottom electrodes. The details of sample preparation can be found in the Methods section. X-ray diffraction (XRD) $\theta-2\theta$ scans indicate epitaxial (001) growth of SAO (Figure S1a), PZT/SAO (Figure 1c), and PZT/LSMO/SAO heterostructures (Figure S2a). The c-axis lattice constant of PZT is 4.15 Å on SAO and 4.18 Å on LSMO buffered SAO, consistent with the compressive strain.[28] Atomic force microscopy (AFM) measurements show the smooth surface morphology of these samples (Figure 1d,
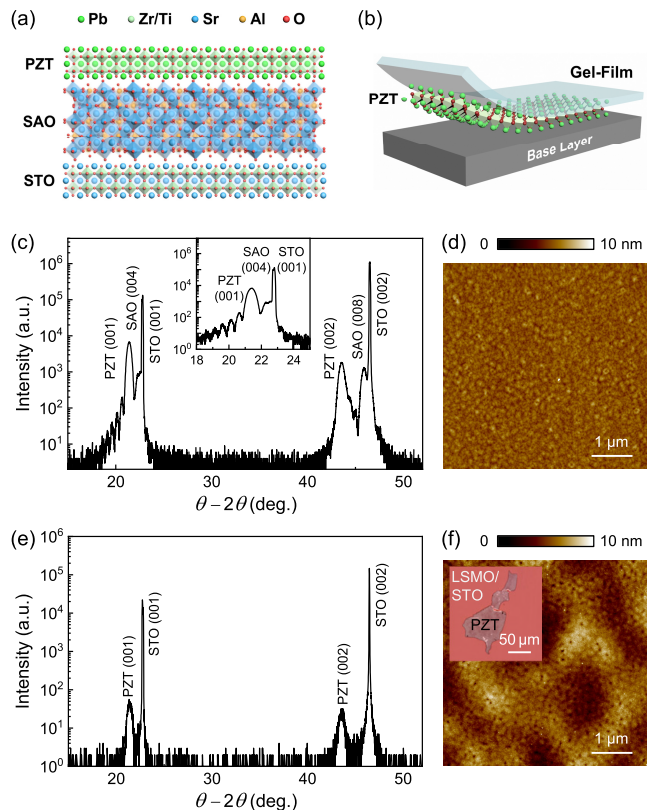

Figure 1. Characterizations of PZT membranes. (a) Schematic of epitaxial PZT/SAO on STO. (b) Schematic view of free-standing PZT membrane transferred on designated base layer via Gel-Film. (c−f) Preparation and characterization of a 50 nm (001) PZT membrane. (c) XRD $\theta-2\theta$ scan with (inset) expanded view showing Laue oscillations around PZT (001) Bragg peak, and (d) AFM topography image of epitaxial PZT/20 nm SAO deposited on STO. (e) XRD $\theta-2\theta$ scan of the same sample after water etching of the SAO buffer layer. (f) AFM topography image of PZT flakes picked up from this sample and transferred on a LSMO/STO base layer. Inset: optical image of the sample.

Figures S1b and Figure S2b), with a typical root-mean-square (RMS) roughness of about 5 Å. Figure 1e shows the XRD $\theta-2\theta$ scan taken on the PZT sample after water etching, which confirms that the SAO buffer layer has been totally removed, while the suspended PZT layer remains single crystalline. The c-axis lattice constant of PZT remains at the same value of 4.15 Å, suggesting that the strained state is sustained even after being separated from the substrate. Selected PZT membrane flakes are then picked up by Gel-Film and transferred onto designated base layers (Figure 1f inset). As shown in Figure 1f, the surface roughness of the PZT membrane transferred on LSMO/STO increases to about 10 Å (Table 1), where surface rippling is clearly visible despite the atomically smooth surface of the base layer. Similarly rippled surface has been observed in previous studies of PZT membranes.[4] Domains written in PZT and PZT/LSMO membranes reveal robust switching between the polarization up (P_{up}) and down (P_{down}) states (Figures S3 and S4).

To further assess the polarization switching of the PZT membranes, we fabricate MoS$_2$ flakes into FETs sandwiched between the free-standing PZT top-gate and SiO$_2$ back-gate (Figure 2a). Figure 2b,c shows the optical images of a MoS$_2$ FET prepared on a SiO$_2$/Si substrate prepatterned with Au electrodes before (Figure 2b) and after a 50 nm free-standing

Table 1. Summary of Properties of PZT and PZT/LSMO Membranes on Different Base Layers[a]

Sample		RMS surface roughness (Å)		E_c (MV cm^{-1})		T_C (°C)
Membrane	Base layer	Membrane	Base layer	P_{up}	P_{down}	
PZT	Au	20 ± 2	7.4 ± 0.1	−3.0 ± 0.2	+1.7 ± 0.1	763 ± 12
	LSMO	10.4 ± 0.6	5.3 ± 0.1	−1.70 ± 0.08	+1.09 ± 0.09	725 ± 25
	MoS$_2$	3.0 ± 0.8	1.1 ± 0.1	−1.60 ± 0.05	+0.75 ± 0.04	588 ± 12
PZT/LSMO	Au	8.0 ± 0.3	7.4 ± 0.1	−0.18 ± 0.04	+0.74 ± 0.05	
	LSMO	5.1 ± 0.3	5.3 ± 0.1	−0.26 ± 0.02	+0.28 ± 0.04	
	MoS$_2$	4.0 ± 0.2	1.1 ± 0.1	-0.6 ± 0.1	+1.01 ± 0.09	

[a]The RMS surface roughness and E_c are deduced from 20 nm membranes. The T_C values are extracted from the thermal quench experiments taken on 50 nm PZT membranes. The error bars for the RMS surface roughness are calculated based on five different locations. The error bars for E_C are calculated based on three cycles of PFM phase switching hysteresis.
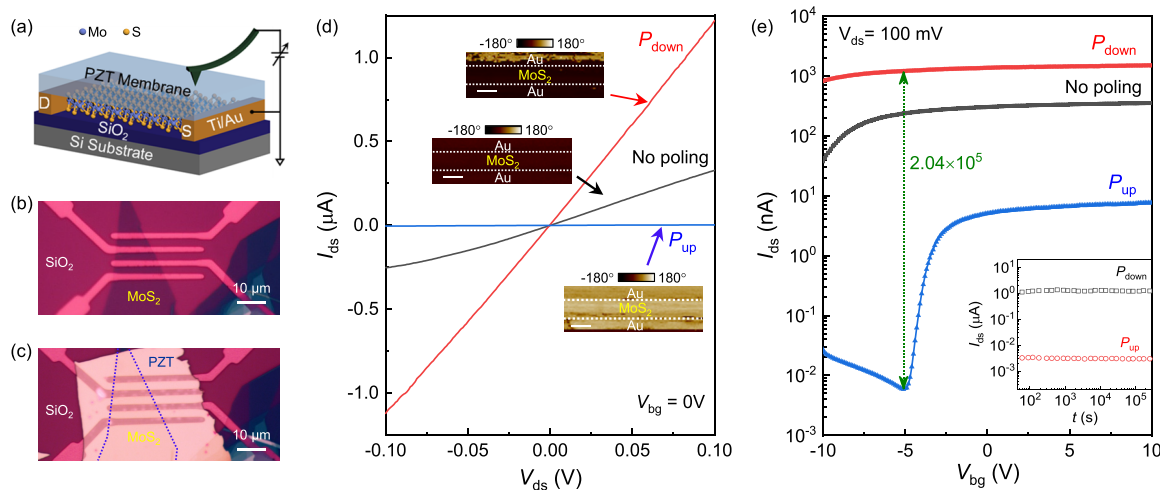

Figure 2. Characterizations of MoS$_2$ FET top-gated by PZT membrane. (a) Device schematic. (b, c) Optical images of a monolayer MoS$_2$ FET on SiO$_2$ before (b) and after (c) a 50 nm PZT membrane transferred on top. The dotted lines outline the edge of MoS$_2$. (d, e) Characterization of a double-gated FL MoS$_2$ FET. (d) Room temperature I_{ds}−V_{ds} taken in the initial no-poling state and after poling into the P_{up} and P_{down} states of PZT top-gate, with (inset) corresponding PFM phase images. Scale bars: 2 μm. (e) Room temperature I_{ds} vs V_{bg} in the initial no-poling state and after poling into the P_{up} and P_{down} states of PZT. Inset: I_{ds} vs time at V_{bg} = 0 V in the on and off states.

PZT membrane transferred on top (Figure 2c). Figure 2d shows the room temperature source drain current (I_{ds}) vs voltage (V_{ds}) relations taken on a 5 nm MoS$_2$ FET at zero back-gate voltage (V_{bg} = 0 V). In the as-prepared state of PZT (no-poling), the device exhibits a linear I−V characteristic, showing an ohmic behavior. We then polarize the PZT region above the channel area into the uniform P_{up} state, which depletes electrons from MoS$_2$. At V_{ds} = 0.1 V, I_{ds} is suppressed by over 2 orders of magnitude, changing from 0.33 μA in the no-poling state to 2.96 nA in the P_{up} state. Switching the polarization of PZT to the P_{down} state accumulates electrons into the channel, enhancing the channel current to 1.22 μA, with a current switching ratio of about 412. Both states show ohmic I−V behavior, and the nonvolatile modulation is consistent with the ferroelectric polarization switching.

Figure 2e shows the transfer characteristics (I_{ds}−V_{bg}) of the FL MoS$_2$ FET for different polarization states at V_{ds} = 0.1 V. For the no-poling state, I_{ds} increases with increasing V_{bg}, indicating that the MoS$_2$ channel is n-type, consistent with that of pristine MoS$_2$.[32] From the quasi-linear dependence of I_{ds}−V_{bg}, we extract the field effect mobility $\mu_{FE} = \frac{L}{CW}\frac{dG}{dV_{bg}}$, where C = 11.5 nF cm^{-2} is the areal capacitance for the 300 nm SiO$_2$ back-gate, $G = I_{ds}/V_{ds}$ is the channel conductance, and $L(W)$ is the channel length (width). The as-prepared sample shows a μ_{FE} of 4.3 cm^2 V^{-1} s^{-1}, comparable with the reported values for

MoS$_2$ FETs with SiO$_2$ back-gates.[32] When the PZT membrane is uniformly polarized to the P_{up} state, I_{ds} is significantly suppressed and decreases exponentially with negative V_{bg}, which corresponds to the subthreshold region with the Fermi level E_F of MoS$_2$ shifted to the midgap region. In the P_{down} state of PZT, the polarization induced high electron doping in MoS$_2$ enhances the channel current to the μA level. I_{ds} shows relatively weak V_{bg}-dependence, indicating that E_F is approaching the conduction band edge with a high density of state. We find that the MoS$_2$ channel cannot be tuned to the subthreshold region by applying a V_{bg} of -40 V in the P_{down} state, which attests to the high doping capacity of crystalline PZT membranes. The current switching ratio between the on (P_{down}) and off (P_{up}) states reaches the highest value of 2.04 × 10^5 at V_{bg} = −5.1 V. For both polarization states, the channel conductance is stable with no appreciable decay for over 3 days (2.6 × 10^5 s) at room temperature (Figure 2e), demonstrating excellent retention behavior. For comparison, MoS$_2$ FETs with a ferroelectric oxide back-gate exhibit antihysteresis behavior and pronounced decay within 10^4 s,[33] which can be attributed to the dynamic response of the interfacial charge layer.[34]

2.2. Polarization Switching and Coercive Fields

We first investigate the effect of the bottom electrode on the polarization switching characteristics of the PZT and PZT/LSMO membranes. Figure 3 shows the PFM switching
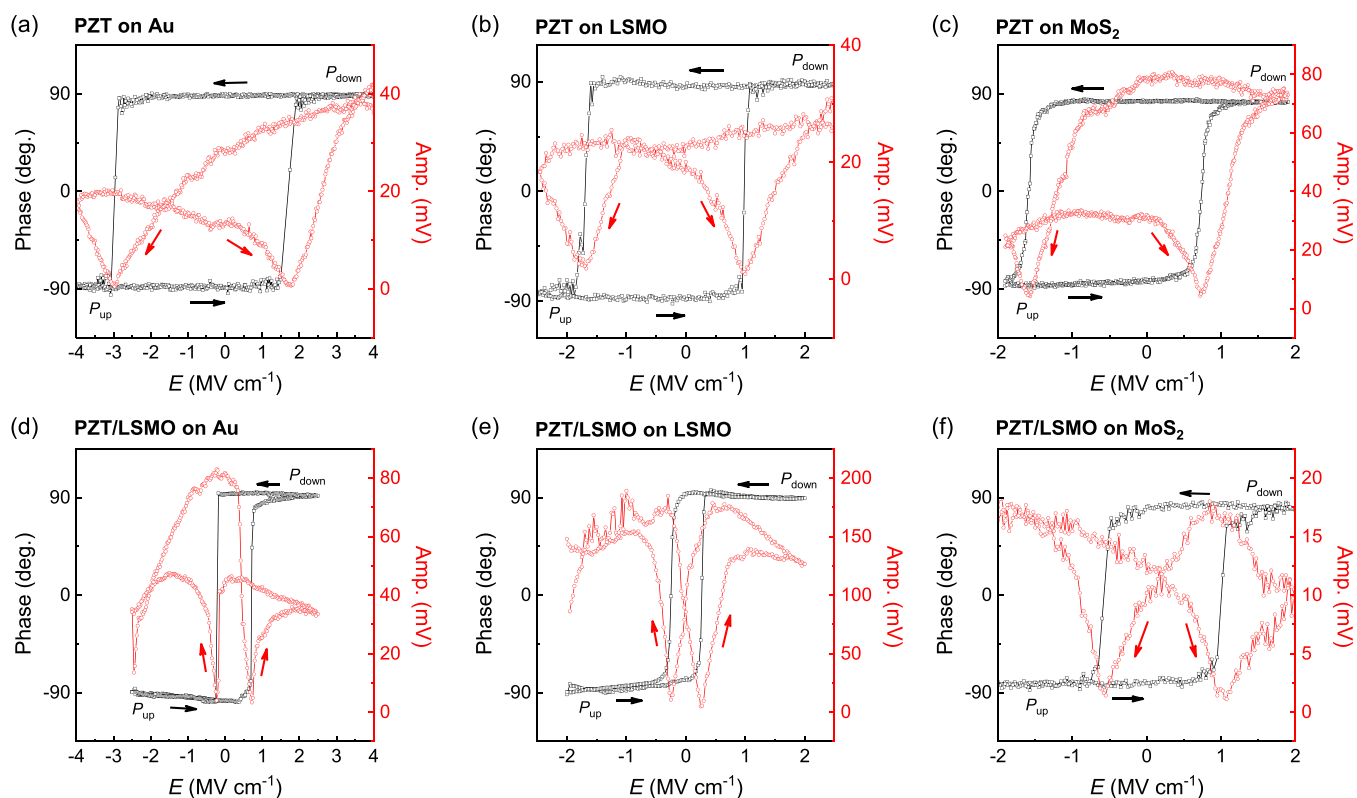
Figure 3. PFM phase and amplitude switching hysteresis for 20 nm PZT and 20 nm PZT/10 nm LSMO membranes on different base layers. (a) PZT on Au. (b) PZT on LSMO. (c) PZT on MoS$_2$. (d) PZT/LSMO on Au. (e) PZT/LSMO on LSMO. (f) PZT/LSMO on MoS$_2$.

hysteresis loops for 20 nm PZT and 20 nm PZT/10 nm LSMO membranes on different base layers, from which we can extract E_c (Table 1). The PFM method has been widely adopted to characterize nanoscale ferroelectrics with limited sizes, such as van der Waals In$_2$Se$_3$[35] and CuInP$_2$O$_6$.[23] Our studies on epitaxial PZT thin films show that the E_c values deduced from the PFM hysteresis is highly consistent with those obtained via the $P(E)$ loop (Supporting Information Section 3).

As summarized in Table 1, for the PZT membranes, E_c is lower for the P_{down} state than for the P_{up} state, suggesting that P_{down} is energetically more favorable. This is consistent with the fact that the as-prepared sample is predominantly in the P_{down} state. The polarization asymmetry has been widely observed in epitaxial PZT thin films, which can be attributed to the asymmetric electrostatic/mechanical boundary conditions.[36] Overall, E_c is the highest for PZT on Au and the lowest for samples on MoS$_2$. As the PZT membranes are in the same strain state, the bottom electrodes can affect E_c through two factors. First, reducing the screening capacity of the bottom electrodes can result in partial screening of the depolarization field, which lowers the ferroelectric double well energy and E_c. For semiconducting electrodes, however, the finite electric field distribution within the electrode reduces the effective voltage applied through PZT,[28] so the net result depends on the competition between these two effects. Second, a higher surface roughness can lead to stronger flexoelectric effect, which reduces the DW velocity and enhances E_c.[4] It is interesting to note that the observed trend for E_c is in line with both the metallicity of the conductive base layer ($E_c(Au) > E_c(LSMO) > E_c(MoS_2)$) and their surface roughness ($RMS(Au) > RMS(LSMO) >$

$RMS(MoS_2)$). This means that we cannot differentiate whether the higher E_c originates from a higher electrode screening capacity or a rougher surface based on this information.

To decouple these two mechanisms, we next investigated the switching hysteresis of the membranes of PZT/LSMO heterostructures, where polarization screening is provided by the epitaxial LSMO layer. The roughness for PZT/LSMO membranes still follows the same trend as that for the base layer. The samples on Au and LSMO are significantly smoother than the corresponding PZT membranes and the one on MoS$_2$ is slightly rougher, suggesting that the presence of LSMO makes the membrane less conformable. The complex interplay of the electrostatic and mechanical boundary conditions is clearly manifested in the following observations:

- The coercive fields for PZT/LSMO membranes are significantly lower than those for PZT membranes on the same base layer, which cannot be simply correlated with the change of electrostatic screening and surface roughness, suggesting interfacial epitaxy plays an important role in determining E_c.

- For PZT/LSMO membranes, despite the fact that all samples have the same screening electrode (LSMO), the E_c value varies strongly on different base layers. The sample on MoS$_2$ possesses the smoothest surface and the highest E_c. The likely scenario is the finite conductivity of semiconducting MoS$_2$ reduces the fractional voltage applied across PZT, effectively increasing E_c.

- The PZT/LSMO membrane on the LSMO base layer exhibits the lowest E_c, which surprisingly is significantly smaller than that of epitaxial PZT/LSMO heterostructures deposited on STO ($-0.5/+1.1$ MV cm^{-1}).[36] As

these two systems possess similar surface roughness, a possible mechanism affecting E_c is the interfacial defect states imposed by substrate clamping effect, which can lead to enhanced DW pining.[30]

- The PZT/LSMO membrane on the LSMO base layer exhibits symmetric coercive fields, while for the PZT/LSMO membranes on Au and MoS$_2$, the polarization asymmetry reverses sign, preferring the P_{up} state. The latter is consistent with the polarization asymmetry observed in epitaxial PZT/LSMO heterostructures deposited on STO substrates.[36]

Overall, the PZT/LSMO membranes transferred on the LSMO/STO base layer exhibit the lowest E_c and symmetric polarization switching behavior, suggesting the existence of competing factors in determining DW pining and polarization switching dynamics. Besides interface screening of depolarization field[28] and roughness induced rippling effect,[4] possible mechanisms include interfacial bonding/reconstruction,[37] defects such as oxygen vacancies,[30,38] and strain,[29] which can tilt the ferroelectric double well energy in opposite directions.

2.3. Domain Wall Pinning and Thermal Roughening

We then investigate the effect of the bottom electrode on the static configuration of DW. The ferroelectric DW can be treated as an elastic manifold roughened by disorder pinning and thermal fluctuation (TF).[39] The DW roughness contains the information about the dimensionality of the system, the type of disorder, and the range of elastic interaction.[36,39–42] The correlation function of the DW displacement u from a straight configuration, $B(L) = \overline{\langle [u(L) - u(0)]^2 \rangle}$, characterizes the thermodynamic and disorder ensemble of the variance of relative displacement between two points separated by a distance L along the DW (Figure 4a). In the elastic regime, $B(L)$ follows a power law dependence: $B(L) \propto L^{2\zeta}$, with ζ being the roughness exponent. Previous studies have shown that DW roughness in epitaxial PZT thin films can be dominated by the 2D RB disorder and thermal fluctuation,[41] corresponding to the roughness exponents of $\zeta_{2D, RB} = 0.31$ and $\zeta_{TF} = 0.5$, respectively, and their competition is strongly affected by the correlated electrode.[36] Theoretically, 1D RB disorder yields an enhanced DW roughness with $\zeta_{1D, RB} = 2/3$, which has not been observed in experimental systems at large length scales (>10 nm), where the dimensionality crossover to 1D DW is always dominated by thermal fluctuation.[36,41,43]

To evaluate the DW roughness, we write oppositely polarized stripe domains on each sample and identify the DW position using the midpoint of the PFM phase response between the P_{up} and P_{down} states (Figure 4b). Figure 4c shows the log−log plot of $B(L)$ calculated from three DWs written on a 50 nm PZT membrane on the LSMO base layer. The typical $B(L)$ follows the power law growth at L smaller than 100 nm, from which we calculate ζ. For each sample, we extract an average ζ value based on 4 to 12 DWs. Figure 4d summarizes the ζ values obtained on 10−50 nm PZT and PZT/LSMO membranes prepared on different base layers. For most samples, the roughness exponent is close to $\zeta_{2D, RB}$, similar to those reported for epitaxial PZT thin films.[36,41] The 10 nm PZT membrane on Au shows a higher ζ, which approaches ζ_{TF} for 1D DW, which suggests thermally activated DW depinning upon the dimensionality crossover.[36] Previous transmission electron microscopy studies of polarization reversal in PZT have revealed the existence of strong polarization pinning at the epitaxial interface,[30] which can be released in the PZT
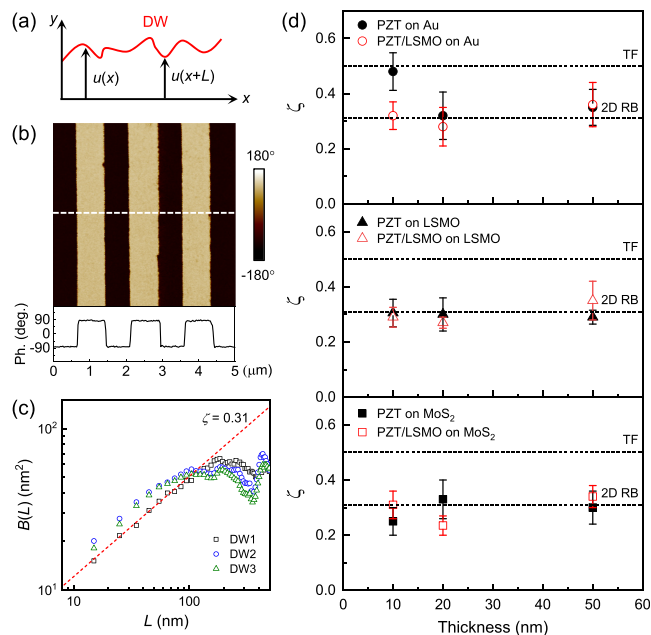

Figure 4. PFM study of DW roughness. (a) DW schematic. (b) PFM phase image of stripe domains written in a 50 nm PZT membrane on LSMO/STO. The lower panel shows the signal profile along the dashed line. (c) Log−log plot of $B(L)$ vs L extracted from three DWs for the sample shown in panel (b). The dashed line corresponds to a fit $\propto L^{2\zeta}$ with $\zeta = 0.31$. (d) ζ vs PZT thickness at room temperature for PZT and PZT/LSMO membranes on different base layers. The dashed lines mark the theoretical ζ values for DW roughening due to 2D RB disorder and TF.

membranes, resulting in lower pinning energy. As the Au substrates possess the highest surface roughness, where the PZT membrane does not fully conform to the substrate morphology, it is plausible that the transition to 1D DW occurs in the 10 nm sample and the thermal energy is sufficient for DW depinning at room temperature. This explains why the higher ζ value is observed only in the PZT membrane on Au.

We then thermally anneal the PZT membranes at progressively higher temperatures and quench the samples to room temperature (Methods). During the rapid cooling, the domain structure does not have sufficient time to reach its thermal equilibrium state, so that the high temperature characteristic can be effectively preserved. In previous studies, we have shown that the thermal quench method yields highly consistent DW roughness with those obtained from high temperature in situ PFM imaging.[36] Figure 5a shows the PFM images of the same set of DWs written on a PZT membrane on Au upon different thermal quench temperatures. The domain structures are stable up to 700 °C, where the DW becomes visibly rougher. At 750 °C, bubble domains emerge in both P_{up} and P_{down} regions, and clear domain structures can no longer be recognized at 775 °C. We thus deduce a T_C of 763 ± 12 °C. Similar temperature dependence has been observed in the PZT membranes on LSMO (Figure 5b) and MoS$_2$ (Figure 5c), with corresponding T_C of 725 ± 25 and 588 ± 12 °C, respectively. Regardless of the bottom electrodes, T_C for the PZT membranes is comparable with those of epitaxial PZT thin films and well above the bulk value,[36] attesting to the strong technological potential for this materials system for high temperature applications.
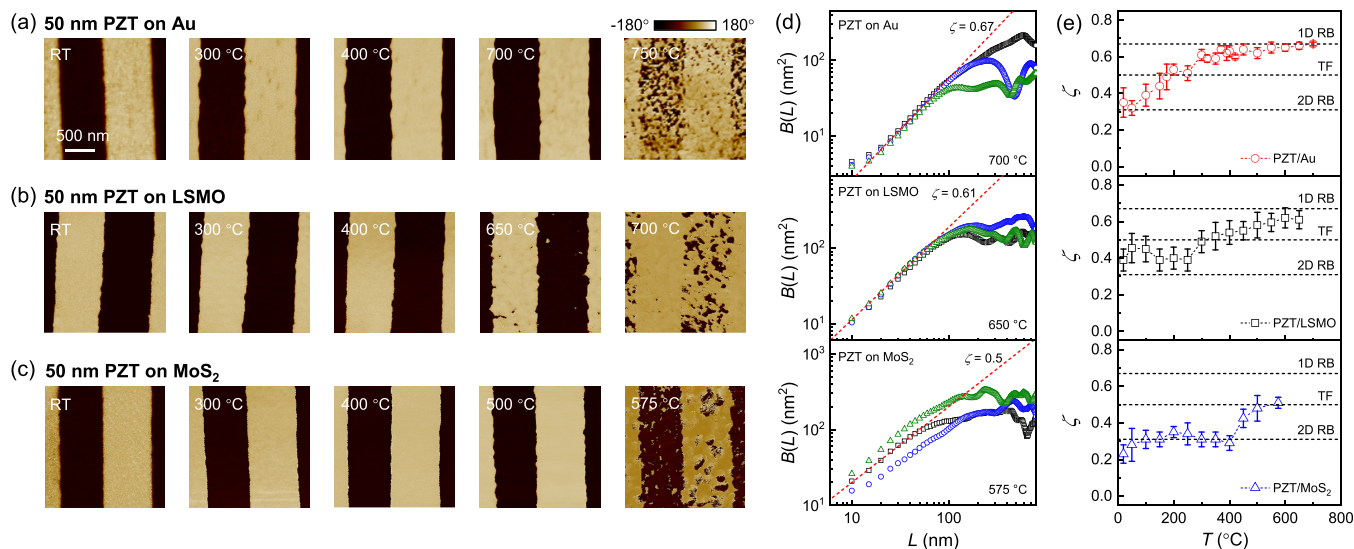
Figure 5. DW roughness upon thermal quench. (a–c) PFM phase images of the same stripe domains at selected thermal quench temperatures for 50 PZT membranes on (a) Au, (b) LSMO, and (c) MoS$_2$. All images are shown at the same scale. (d) Log–log plot of $B(L)$ *vs* L extracted from selected DWs for PZT membranes on different base layers at high temperatures. The dashed lines correspond to fits $\propto L^{2\zeta}$ with ζ values labeled. (e) ζ *vs* T for PZT membranes on different base layers. The dashed lines mark the ζ theoretical values for DW roughening due to 2D RB disorder, TF, and 1D RB disorder.

For all samples, the DWs became rougher at high temperatures. Figure 5d shows the $B(L)$ *vs* L extracted from DWs for 50 nm PZT membranes on different base layers after high temperature thermal quench. As shown in Figure 5e, ζ increases gradually with the thermal quench temperature. For PZT on MoS$_2$, ζ starts to deviate from $\zeta_{2D, RB}$ at a crossover temperature T_{cr} = 400 °C and saturates at ζ_{TF} close to T_C, which is similar to epitaxial PZT films. This temperature dependence reflects a dimensionality crossover from 2D to 1D when the thermal energy is larger than the disorder pinning energy. For PZT on LSMO and Au, despite their much higher T_C, ζ starts to increase at much lower T_{cr} values of 250 °C and room temperature, respectively, suggesting the existence of DW trapping sites with shallow well energy.[36] Previous PFM studies of epitaxial PZT/LSMO heterostructures reveal a high T_{cr} of 450−500 °C, which has been attributed to the migration of oxygen vacancies supplied by the LSMO electrode as well as substrate clamping effect; a much lower T_{cr} close to room temperature has been observed in epitaxial PZT/SrIrO$_3$ heterostructures, with the pseudocubic SrIrO$_3$ possessing higher energy barrier for oxygen vacancy migration and imposing less lattice clamping.[36] Both the DW pinning and substrate clamping scenarios can account for the relatively low T_{cr} observed in the PZT membranes on LSMO and Au. For the former mechanism, the absence of interfacial atomic bonding imposes a natural barrier for oxygen migration between the LSMO and PZT membrane, and Au cannot serve as an oxygen reservoir. Another critical factor is the rippling induced flexoelectric effect, which further suppresses the mobility of charged disorders (e.g., oxygen vacancies). For the latter mechanism, the much smoother surface morphology of the PZT membranes compared with the LSMO and Au base layers (Table 1) suggests that the interface is constituted of a network of point contacts rather than a fully conformed surface, which facilitates strain release. In contrast, the flat interface for the PZT membrane on MoS$_2$ not only facilitates the migration of charged defects but also helps preserve the original strain state of the sample, thus resulting in a much

higher T_{cr}. It is expected that these mechanisms become increasingly dominant in thinner membranes, which explains the yet lower T_{cr} (below room temperature) observed in the 10 nm PZT membrane on Au (Figure 4d).

At high temperature, ζ for the 50 nm PZT membranes on Au and LSMO settles at $\zeta_{1D, RB}$, consistent with the creep motion model within quasi-equilibrium-nucleation picture.[44] Such high $\zeta_{1D, RB}$ has not been observed in epitaxial PZT films at a large length scale, where the 1D DW is dominated by thermal roughening and cannot fully equilibrate according to the disorder landscape. For PZT membranes on a relatively rough interface, the local flexoelectric field facilitates the DW to settle upon the disordered potential and suppresses thermal fluctuation, allowing the DW roughness to be dominated by the 1D RB disorder.

3. CONCLUSIONS

In summary, we have investigated the effects of electrostatic and mechanical boundary conditions on the polarization switching behavior and DW configuration of high-quality freestanding PZT and PZT/LSMO membranes prepared on different bottom electrodes: metallic Au, correlated oxide LSMO, and 2D semiconductor MoS$_2$. All samples show robust ferroelectric switching, and the PZT membranes exhibit T_C values well above the bulk value. PFM studies reveal the collective effects of the screening capacity, surface roughness, defect state, and interfacial epitaxy of the bottom electrode in determining the coercive field, Curie temperature, and domain wall roughness of the PZT membranes. The polarization switching in PZT induces nonvolatile current switching in few-layer MoS$_2$ FETs, with an on/off ratio up to 2.04 × 10^5 achieved at room temperature. Our study provides important material parameters for designing PZT membrane-based nanoelectronic devices, paving the path for their implementation in programmable, flexible nonvolatile memory, neuromorphic computing, and optoelectronic applications.

METHODS

Sample Preparation

Epitaxial 10−50 nm PZT thin films and PZT/10 nm LSMO heterostructures were deposited on 20 nm SAO buffered (001) STO substrates by using off-axis radio frequency magnetron sputtering. For SAO, LSMO, and PZT layers, the growth temperatures/process gas conditions were 650 °C/10 mTorr processing gas (Ar:O_2 = 1:8), 650 °C/150 mTorr processing gas (Ar:O_2 = 2:1), and 500 °C/120 mTorr processing gas (Ar:O_2 = 2:1), respectively. The samples were then immersed into deionized water at room temperature for about 2 h to dissolve the SAO buffer layer. After being dried, selected membrane flakes were picked up by Gel-Film on a microscope stage. After 50 °C heating for 5 min, the Gel-Film with the PZT or PZT/LSMO membranes attached was slowly detached from the STO substrate and placed on three types of base layers, 20−50 nm Au coated SiO_2/Si, 20 nm LSMO deposited on (001) STO substrates, and FL MoS_2 flakes exfoliated on SiO_2/Si, which serve as the bottom electrodes. The Gel-Film was then released slowly, with the PZT or PZT/LSMO membrane staying on the conducting base layers.

Sample Characterization

XRD measurements were performed using a Rigaku SmartLab Diffractometer (3 kW Cu Kα source, Ge(220)x2 monochromator and analyzer). The AFM and PFM measurements were taken using a Bruker Multimode 8 AFM. To write the domain structures, we applied a bias voltage (V_{bias}) larger than the film's coercive voltage between a scanning conductive AFM probe (NanoSensors PPP-EFM, Pt/Ir-coated probe) and the bottom electrode. To image the domain structures, we conducted PFM close to the resonance frequency of the cantilever (370 ± 30 kHz). For the thermal quench experiments, the samples were heated to progressively higher temperatures in a Muffle Furnace (Thermo Scientific FB1315M) in no-overshoot mode. After being heated for 30 min at the settled temperature, the sample was placed on a large metal plate to quench it to room temperature rapidly. The resulting domain structures were imaged at room temperature.

Device Fabrication and Electrical Measurements

To fabricate the MoS_2 FET, we first fabricated electrode patterns in two-point geometry on 300 nm SiO_2/p-type Si substrates using photolithography and deposited 10 nm Au/2 nm Ti via e-beam evaporation. Mechanically exfoliated FL MoS_2 flakes were transferred onto the prepatterned electrodes via Gel-Film. We then transferred 50 nm free-standing PZT membranes on MoS_2. The samples were thermally annealed in Ar gas at 200 °C for 120 min to improve the interface contact. The electrical measurements were performed using the Semiconductor Device Parameter Analyzer (Keysight B1500A) at room temperature.

ASSOCIATED CONTENT

Ⓢ Supporting Information

The Supporting Information is available free of charge at https://pubs.acs.org/doi/10.1021/acsnanoscienceau.3c00032.

> Structural and surface characterization of $Sr_3Al_2O_6$-buffered heterostructures; PFM characterization of PZT and PZT/LSMO membranes on different base layers; comparison of coercive field of PZT deduced from PFM hysteresis and $P-E$ loops (PDF)

AUTHOR INFORMATION

Corresponding Author

Xia Hong − *Department of Physics and Astronomy & Nebraska Center for Materials and Nanoscience, University of Nebraska−Lincoln, Lincoln, Nebraska 68588-0299, United States;* ⓞ orcid.org/0000-0002-7873-5774; Email: xia.hong@unl.edu

Authors

Qiuchen Wu − *Department of Physics and Astronomy & Nebraska Center for Materials and Nanoscience, University of Nebraska−Lincoln, Lincoln, Nebraska 68588-0299, United States*

Kun Wang − *Department of Physics and Astronomy & Nebraska Center for Materials and Nanoscience, University of Nebraska−Lincoln, Lincoln, Nebraska 68588-0299, United States;* ⓞ orcid.org/0000-0001-6127-349X

Alyssa Simpson − *Department of Physics and Astronomy & Nebraska Center for Materials and Nanoscience, University of Nebraska−Lincoln, Lincoln, Nebraska 68588-0299, United States*

Yifei Hao − *Department of Physics and Astronomy & Nebraska Center for Materials and Nanoscience, University of Nebraska−Lincoln, Lincoln, Nebraska 68588-0299, United States*

Jia Wang − *Department of Physics and Astronomy & Nebraska Center for Materials and Nanoscience, University of Nebraska−Lincoln, Lincoln, Nebraska 68588-0299, United States;* ⓞ orcid.org/0000-0002-2213-6203

Dawei Li − *Department of Physics and Astronomy & Nebraska Center for Materials and Nanoscience, University of Nebraska−Lincoln, Lincoln, Nebraska 68588-0299, United States;* ⓞ orcid.org/0000-0001-6967-4968

Complete contact information is available at: https://pubs.acs.org/10.1021/acsnanoscienceau.3c00032

Author Contributions

CRediT: **Qiuchen Wu** data curation, formal analysis, validation, writing-original draft; **Kun Wang** data curation, formal analysis; **Alyssa Simpson** data curation; **Yifei Hao** data curation; **Jia Wang** data curation; **Dawei Li** data curation, formal analysis; **Xia Hong** conceptualization, formal analysis, funding acquisition, supervision, writing-original draft.

Notes

The authors declare no competing financial interest.

ACKNOWLEDGMENTS

REFERENCES

(1) Lee, D. Flexoelectricity in thin films and membranes of complex oxides. *APL Materials* **2020**, *8* (9), No. 090901.

(2) Pesquera, D.; Fernandez, A.; Khestanova, E.; Martin, L. W. Freestanding complex-oxide membranes. *J. Phys.: Condens. Matter* **2022**, *34* (38), 383001.

(3) Ji, J.; Park, S.; Do, H.; Kum, H. S. A review on recent advances in fabricating freestanding single-crystalline complex-oxide membranes and its applications. *Phys. Scr.* **2023**, *98* (5), No. 052002.

(4) Bakaul, S. R.; Kim, J.; Hong, S.; Cherukara, M. J.; Zhou, T.; Stan, L.; Serrao, C. R.; Salahuddin, S.; Petford-Long, A. K.; Fong, D. D.;

Holt, M. V. Ferroelectric Domain Wall Motion in Freestanding Single-Crystal Complex Oxide Thin Film. *Adv. Mater.* **2020**, *32* (4), 1907036.

(5) Elangovan, H.; Barzilay, M.; Seremi, S.; Cohen, N.; Jiang, Y.; Martin, L. W.; Ivry, Y. Giant Superelastic Piezoelectricity in Flexible Ferroelectric BaTiO$_3$ Membranes. *ACS Nano* **2020**, *14* (4), 5053−5060.

(6) Li, Y.; Zatterin, E.; Conroy, M.; Pylypets, A.; Borodavka, F.; Björling, A.; Groenendijk, D. J.; Lesne, E.; Clancy, A. J.; Hadjimichael, M.; Kepaptsoglou, D.; Ramasse, Q. M.; Caviglia, A. D.; Hlinka, J.; Bangert, U.; Leake, S. J.; Zubko, P. Electrostatically Driven Polarization Flop and Strain-Induced Curvature in Free-Standing Ferroelectric Superlattices. *Adv. Mater.* **2022**, *34* (15), 2106826.

(7) Han, L.; Yang, X.; Lun, Y.; Guan, Y.; Huang, F.; Wang, S.; Yang, J.; Gu, C.; Gu, Z. B.; Liu, L.; Wang, Y.; Wang, P.; Hong, J.; Pan, X.; Nie, Y. Tuning Piezoelectricity via Thermal Annealing at a Freestanding Ferroelectric Membrane. *Nano Lett.* **2023**, *23* (7), 2808−2815.

(8) Han, L.; Addiego, C.; Prokhorenko, S.; Wang, M.; Fu, H.; Nahas, Y.; Yan, X.; Cai, S.; Wei, T.; Fang, Y.; Liu, H.; Ji, D.; Guo, W.; Gu, Z.; Yang, Y.; Wang, P.; Bellaiche, L.; Chen, Y.; Wu, D.; Nie, Y.; Pan, X. High-density switchable skyrmion-like polar nanodomains integrated on silicon. *Nature* **2022**, *603* (7899), 63−67.

(9) Bakaul, S. R.; Prokhorenko, S.; Zhang, Q.; Nahas, Y.; Hu, Y.; Petford-Long, A.; Bellaiche, L.; Valanoor, N. Freestanding Ferroelectric Bubble Domains. *Adv. Mater.* **2021**, *33* (45), 2105432.

(10) Jiang, X.; Liu, Y.; Zang, Y.; Liu, Y.; Gao, T.; Zheng, N.; Gu, Z.; Yang, Y.; Wu, D.; Nie, Y. Uniaxial strain induced anisotropic bandgap engineering in freestanding BiFeO$_3$ films. *APL Mater.* **2022**, *10* (9), No. 091110.

(11) Wang, Q.; Wang, J.; Fang, H.; Chen, Y.; Han, Y.; Liu, H.; Wang, D.; Zhang, P.; Shi, C.; Guo, J.; He, B.; Zheng, L.; Lü, W. Polarization Evolution in Morphology-Engineered Freestanding Single-Crystalline BaTiO$_3$ Membranes. *J. Phys. Chem. C* **2022**, *126* (38), 16369−16376.

(12) Pesquera, D.; Parsonnet, E.; Qualls, A.; Xu, R.; Gubser, A. J.; Kim, J.; Jiang, Y.; Velarde, G.; Huang, Y.; Hwang, H. Y.; Ramesh, R.; Martin, L. W. Beyond Substrates: Strain Engineering of Ferroelectric Membranes. *Adv. Mater.* **2020**, *32* (43), 2003780.

(13) Han, L.; Fang, Y.; Zhao, Y.; Zang, Y.; Gu, Z.; Nie, Y.; Pan, X. Giant Uniaxial Strain Ferroelectric Domain Tuning in Freestanding PbTiO$_3$ Films. *Adv. Mater. Interfaces* **2020**, *7* (7), 1901604.

(14) Guo, R.; You, L.; Lin, W.; Abdelsamie, A.; Shu, X.; Zhou, G.; Chen, S.; Liu, L.; Yan, X.; Wang, J.; Chen, J. Continuously controllable photoconductance in freestanding BiFeO$_3$ by the macroscopic flexoelectric effect. *Nat. Commun.* **2020**, *11* (1), 2571.

(15) Lin, A.; Hong, X.; Wood, V.; Verevkin, A. A.; Ahn, C. H.; McKee, R. A.; Walker, F. J.; Specht, E. D. Epitaxial growth of Pb(Zr$_{0.2}$Ti$_{0.8}$)O$_3$ on Si and its nanoscale piezoelectric properties. *Appl. Phys. Lett.* **2001**, *78* (14), 2034−2036.

(16) Lu, D.; Crossley, S.; Xu, R.; Hikita, Y.; Hwang, H. Y. Freestanding Oxide Ferroelectric Tunnel Junction Memories Transferred onto Silicon. *Nano Lett.* **2019**, *19* (6), 3999−4003.

(17) Luo, Z. D.; Peters, J. J. P.; Sanchez, A. M.; Alexe, M. Flexible Memristors Based on Single-Crystalline Ferroelectric Tunnel Junctions. *ACS Appl. Mater. Interfaces* **2019**, *11* (26), 23313−23319.

(18) Li, D.; Huang, X.; Wu, Q.; Zhang, L.; Lu, Y.; Hong, X. Ferroelectric Domain Control of Nonlinear Light Polarization in MoS$_2$ via PbZr$_{0.2}$Ti$_{0.8}$O$_3$ Thin Films and Free-Standing Membranes. *Adv. Mater.* **2023**, *35* (9), 2208825.

(19) Puebla, S.; Pucher, T.; Rouco, V.; Sanchez-Santolino, G.; Xie, Y.; Zamora, V.; Cuellar, F. A.; Mompean, F. J.; Leon, C.; Island, J. O.; Garcia-Hernandez, M.; Santamaria, J.; Munuera, C.; Castellanos-Gomez, A. Combining Freestanding Ferroelectric Perovskite Oxides with Two-Dimensional Semiconductors for High Performance Transistors. *Nano Lett.* **2022**, *22* (18), 7457−7466.

(20) Jia, X.; Guo, R.; Tay, B. K.; Yan, X. Flexible Ferroelectric Devices: Status and Applications. *Adv. Funct. Mater.* **2022**, *32* (45), 2205933.

(21) Han, S.; Meng, Y.; Xu, Z.; Kim, J. S.; Li, Y.; Roh, I.-P.; Ahn, H.; Kim, D.-H.; Bae, S.-H. Freestanding Membranes for Unique Functionality in Electronics. *ACS Appl. Electron. Mater.* **2023**, *5* (2), 690−704.

(22) Ducharme, S.; Palto, S. P.; Freidkin, V. M.; Blinov, L. M. *Ferroelectric Polymer Langmuir-Blodgett Films*. Academic Press: San Diego, 2002; Vol. 3.

(23) Wang, K.; Li, D.; Wang, J.; Hao, Y.; Anderson, H.; Yang, L.; Hong, X. Interface-Tuning of Ferroelectricity and Quadruple-Well State in CuInP$_2$S$_6$ via Ferroelectric Oxide. *ACS Nano* **2023**, *17* (16), 15787−15795.

(24) Zhao, Z.; Abdelsamie, A.; Guo, R.; Shi, S.; Zhao, J.; Lin, W.; Sun, K.; Wang, J.; Wang, J.; Yan, X.; Chen, J. Flexible artificial synapse based on single-crystalline BiFeO$_3$ thin film. *Nano Res.* **2022**, *15* (3), 2682−2688.

(25) Sun, H.; Wang, J.; Wang, Y.; Guo, C.; Gu, J.; Mao, W.; Yang, J.; Liu, Y.; Zhang, T.; Gao, T.; Fu, H.; Zhang, T.; Hao, Y.; Gu, Z.; Wang, P.; Huang, H.; Nie, Y. Nonvolatile ferroelectric domain wall memory integrated on silicon. *Nat. Commun.* **2022**, *13* (1), 4332.

(26) Liu, H.; Zhu, W.; Mao, Q.; Peng, B.; Xu, Y.; Dong, G.; Chen, B.; Peng, R.; Zhao, Y.; Zhou, Z.; Yang, S.; Huang, H.; Liu, M. Single-Crystalline BaZr$_{0.2}$Ti$_{0.8}$O$_3$ Membranes Enabled High Energy Density in PEI-Based Composites for High-Temperature Electrostatic Capacitors. *Adv. Mater.* **2023**, *35* (22), 2300962.

(27) Fong, D. D.; Kolpak, A. M.; Eastman, J. A.; Streiffer, S. K.; Fuoss, P. H.; Stephenson, G. B.; Thompson, C.; Kim, D. M.; Choi, K. J.; Eom, C. B.; Grinberg, I.; Rappe, A. M. Stabilization of monodomain polarization in ultrathin PbTiO$_3$ films. *Phys. Rev. Lett.* **2006**, *96* (12), No. 127601.

(28) Hao, Y.; Li, T.; Yun, Y.; Li, X.; Chen, X.; Song, J.; Ahmadi, Z.; Shield, J. E.; Xu, X.; Hong, X. Tuning Negative Capacitance in PbZr$_{0.2}$Ti$_{0.8}$O$_3$/SrTiO$_3$ Heterostructures via Layer Thickness Ratio. *Phys. Rev. Appl.* **2021**, *16* (3), No. 034004.

(29) Damodaran, A. R.; Agar, J. C.; Pandya, S.; Chen, Z.; Dedon, L.; Xu, R.; Apgar, B.; Saremi, S.; Martin, L. W. New modalities of strain-control of ferroelectric thin films. *J. Phys.: Condens. Matter* **2016**, *28* (26), No. 263001.

(30) Han, M. G.; Marshall, M. S. J.; Wu, L.; Schofield, M. A.; Aoki, T.; Twesten, R.; Hoffman, J.; Walker, F. J.; Ahn, C. H.; Zhu, Y. Interface-induced nonswitchable domains in ferroelectric thin films. *Nat. Commun.* **2014**, *5*, 4693.

(31) Dawber, M.; Rabe, K. M.; Scott, J. F. Physics of thin-film ferroelectric oxides. *Rev. Modern Phys.* **2005**, *77* (4), 1083.

(32) Zhu, W.; Low, T.; Lee, Y. H.; Wang, H.; Farmer, D. B.; Kong, J.; Xia, F.; Avouris, P. Electronic transport and device prospects of monolayer molybdenum disulphide grown by chemical vapour deposition. *Nat. Commun.* **2014**, *5*, 3087.

(33) Zhang, X. W.; Xie, D.; Xu, J. L.; Sun, Y. L.; Li, X.; Zhang, C.; Dai, R. X.; Zhao, Y. F.; Li, X. M.; Li, X.; Zhu, H. W. MoS$_2$ Field-Effect Transistors With Lead Zirconate-Titanate Ferroelectric Gating. *IEEE Electron Device Lett.* **2015**, *36* (8), 784−786.

(34) Hong, X.; Hoffman, J.; Posadas, A.; Zou, K.; Ahn, C. H.; Zhu, J. Unusual resistance hysteresis in *n*-layer graphene field effect transistors fabricated on ferroelectric Pb(Zr$_{0.2}$Ti$_{0.8}$)O$_3$. *Appl. Phys. Lett.* **2010**, *97* (3), No. 033114.

(35) Io, W. F.; Yuan, S.; Pang, S. Y.; Wong, L. W.; Zhao, J.; Hao, J. Temperature- and thickness-dependence of robust out-of-plane ferroelectricity in CVD grown ultrathin van der Waals α-In$_2$Se$_3$ layers. *Nano Res.* **2020**, *13* (7), 1897−1902.

(36) Wang, K.; Hao, Y.; Zhang, L.; Zhang, Y.; Chen, X.; Hong, X. Effect of correlated oxide electrodes on disorder pinning and thermal roughening of ferroelectric domain walls in epitaxial PbZr$_{0.2}$Ti$_{0.8}$O$_3$ thin films. *Phys. Rev. Mater.* **2021**, *5* (7), No. 074402.

(37) Gao, P.; Liu, H. J.; Huang, Y. L.; Chu, Y. H.; Ishikawa, R.; Feng, B.; Jiang, Y.; Shibata, N.; Wang, E. G.; Ikuhara, Y. Atomic mechanism of polarization-controlled surface reconstruction in ferroelectric thin films. *Nat. Commun.* **2016**, *7*, 11318.

(38) Kim, Y. M.; Morozovska, A.; Eliseev, E.; Oxley, M. P.; Mishra, R.; Selbach, S. M.; Grande, T.; Pantelides, S. T.; Kalinin, S. V.;

Borisevich, A. Y. Direct observation of ferroelectric field effect and vacancy-controlled screening at the $BiFeO_3/La_xSr_{1-x}MnO_3$ interface. *Nat. Mater.* **2014**, *13* (11), 1019−1025.

(39) Emig, T.; Nattermann, T. Disorder driven roughening transitions of elastic manifolds and periodic elastic media. *Eur. Phys. J. B* **1999**, *8* (4), 525−546.

(40) Agoritsas, E.; Lecomte, V.; Giamarchi, T. Temperature-induced crossovers in the static roughness of a one-dimensional interface. *Phys. Rev. B* **2010**, *82* (18), No. 184207.

(41) Paruch, P.; Kolton, A. B.; Hong, X.; Ahn, C. H.; Giamarchi, T. Thermal quench effects on ferroelectric domain walls. *Phys. Rev. B* **2012**, *85* (21), No. 214115.

(42) Xiao, Z.; Poddar, S.; Ducharme, S.; Hong, X. Domain wall roughness and creep in nanoscale crystalline ferroelectric polymers. *Appl. Phys. Lett.* **2013**, *103* (11), 112903.

(43) Guyonnet, J.; Agoritsas, E.; Bustingorry, S.; Giamarchi, T.; Paruch, P. Multiscaling Analysis of Ferroelectric Domain Wall Roughness. *Phys. Rev. Lett.* **2012**, *109* (14), No. 147601.

(44) Kolton, A. B.; Rosso, A.; Giamarchi, T. Creep Motion of an Elastic String in a Random Potential. *Phys. Rev. Lett.* **2005**, *94* (4), No. 047002.